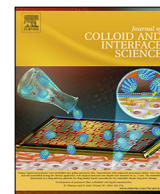




Contents lists available at ScienceDirect

Journal of Colloid and Interface Science

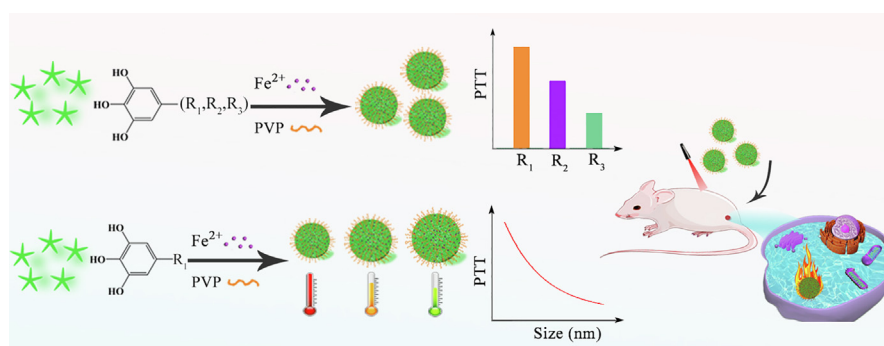
journal homepage: [www.elsevier.com/locate/jcis](http://www.elsevier.com/locate/jcis)

## Regular Article

## Controllable synthesis of iron-polyphenol colloidal nanoparticles with composition-dependent photothermal performance

Jing Qin<sup>a</sup>, Guohai Liang<sup>b</sup>, Dong Cheng<sup>a</sup>, Yining Liu<sup>a</sup>, Xiaoran Cheng<sup>a</sup>, Pengkun Yang<sup>a</sup>, Na Wu<sup>a</sup>, Yongxi Zhao<sup>a</sup>, Jing Wei<sup>a,\*</sup><sup>a</sup> Institute of Analytical Chemistry and Instrument for Life Science, The Key Laboratory of Biomedical Information Engineering of Ministry of Education, School of Life Science and Technology, Xi'an Jiaotong University, Xi'an, Shaanxi 710049, China<sup>b</sup> College of Biophotonics, South China Normal University, Guangzhou 510631, China

## GRAPHICAL ABSTRACT



## ARTICLE INFO

## Article history:

Received 16 December 2020

Revised 17 February 2021

Accepted 18 February 2021

Available online 9 March 2021

## Keywords:

Polyphenol

Photothermal therapy

Colloidal sphere

Iron-polyphenol complex

Self-assembly

## ABSTRACT

Iron-polyphenol nanoparticles are usually prepared with nontoxic plant polyphenols as a main building block, which are an emerging photothermal agent for photothermal therapy. However, till now, few works have been made on the controllable synthesis of iron-polyphenol nanoparticles with tunable composition, as well as investigation of the relationship between material composition and photothermal property. In the present study, iron-polyphenol colloidal nanoparticles with tunable diameter (21–303 nm) and iron content (9.2–97.6 mg/g), as well as high colloidal stability are successfully synthesized using different polyphenols (such as tannic acid, epigallocatechin gallate, gallic acid, epicatechin and proanthocyanidin) as a ligand. In addition, photothermal performance is highly dependent on the organic ligand, iron content and particle size. Higher iron content and smaller diameter can contribute to higher photothermal performance. The iron-polyphenol nanoparticles with the optimal iron content and particle size are selected as a photothermal agent. They can effectively inhibit the tumour growth *in vivo*. The current work demonstrates a general synthesis strategy for iron-polyphenol colloidal nanoparticles with tailorable composition and clarifies the relationship between material composition and photothermal performance. Moreover, it is conducive to the rational design of polyphenol-based photothermal agents for theranostic applications.

© 2021 Elsevier Inc. All rights reserved.

\* Corresponding author.

E-mail address: [jingwei@xjtu.edu.cn](mailto:jingwei@xjtu.edu.cn) (J. Wei).

## 1. Introduction

Photothermal therapy (PTT) has been considered an efficient cancer therapy technique. It employs photothermal agents (PTAs) to induce local hyperthermia in order to ablate tumours under light irradiation [1–3]. PTT technique exhibits advantages containing high therapeutic selectivity, minimal side effects and non-invasiveness [4–5]. Under near-infrared (NIR) laser irradiation, the tumour with accumulation of PTAs can only be eliminated. The features such as good biocompatibility and high photothermal performance are proved to be key parameters for an excellent photothermal agent. Till the present, different PTAs including metal nanoparticles (e.g., Au) [6–8], carbon nanomaterials (e.g., carbon nanotubes, carbon nanoparticles and graphene) [9–11], polymers (e.g., polydopamine, polypyrrole) [12–13] and semiconductor nanomaterials (e.g., MoS<sub>2</sub> and WS<sub>2</sub>) [14–15] have been developed. Despite great progresses on the development of PTAs, there remains enormous room to improve PTAs in biocompatibility, photothermal performance and multi-functions [16–20].

Polyphenols refer to water-soluble plant phenolic compounds. Besides, they reveal different biological functions including chemical defense, structural support, pigmentation and prevention of radiation damage [21–25]. Due to the low cost, nontoxicity, renewability and strong metal-chelating ability of polyphenol, various metal-polyphenol nanoparticles have been prepared. Such metal-polyphenol nanoparticles exhibit widespread applications in biomedicine, bioimaging, biosensor, catalysis, energy conversion and storage [26–43]. Iron-polyphenol nanoparticles present excellent biocompatibility, efficient photothermal performance and broad applications in imaging-guided therapy [44–54]. For example, Liu *et al.* [44] prepared iron-gallic acid coordination polymer nanodots (~5.3 nm). The nanodots can be employed in T<sub>1</sub>-weighted magnetic resonance imaging (MRI) and PTT. Zhao *et al.* [45] synthesized nanoscale iron-ellagic acid coordination crystals with rhombohedral morphology (~240 nm) for T<sub>2</sub>-weighted MRI and PTT. Our group prepared bimetal (Gd/Fe)-tannic acid polymer nanoparticles with tunable Gd/Fe ratio and ultra-small diameter (~23 nm) for T<sub>1</sub>-weighted MRI and PTT [46]. Liu *et al.* [47] reported nanovesicle-supported iron-tannic acid for tumour-specific photoactivated application, like PTT, photothermal imaging, photoacoustic imaging and T<sub>1</sub>-weighted MRI. Based on the above progresses, iron-polyphenol nanoparticles have revealed promising theranostic applications. However, the reported iron-polyphenol nanoparticles usually showed uncontrollable particle size and monotonous composition. The particle size and composition of iron-polyphenol nanoparticles exert conspicuous effect on their photothermal performance. Till now, over 8000 phenolic compounds with various chemical structures and functions have been found in plant tissues [26]. These polyphenols may endow the iron-polyphenol complex with new functions. To further explore the functions and applications of metal-polyphenol nanoparticles, a general method for controllable synthesis of metal-polyphenol colloidal nanoparticles using different polyphenol ligands is highly required. Moreover, it is beneficial to understanding the relationships between the composition of iron-polyphenol complex and photothermal performance. For all we know, there are extremely few works on the controllable synthesis of iron-polyphenol nanoparticles with tunable composition and particle size, as well as investigation of the relationship between composition and photothermal performance of polyphenol-based photothermal agents.

In the current work, a general synthesis strategy is developed for iron-polyphenol colloidal nanoparticles using five different polyphenols as a chelating ligand (Scheme 1), including tannic acid

(TA), epigallocatechin gallate (EGCG), gallic acid (GA), epicatechin (EC) and proanthocyanidin (PAC). The iron-polyphenol colloidal nanoparticles demonstrate tunable diameter (21–303 nm) and iron content (9.2–97.6 mg/g), as well as high colloidal stability. Subsequently, the relationship between composition and photothermal performance is systematically investigated. The factors including the kind of polyphenol ligand, Fe content in the complex and particle size can obviously affect the photothermal performance of the iron-polyphenol colloidal nanoparticles. In addition, a high iron content and small diameter can effectively enhance the photothermal performance. Iron-tannic acid colloidal nanoparticles with optimized composition are selected as a typical photothermal agent. Moreover, they can be successfully used to kill cancer cell *in vitro* and *in vivo*.

## 2. Materials and methods

### 2.1. Materials

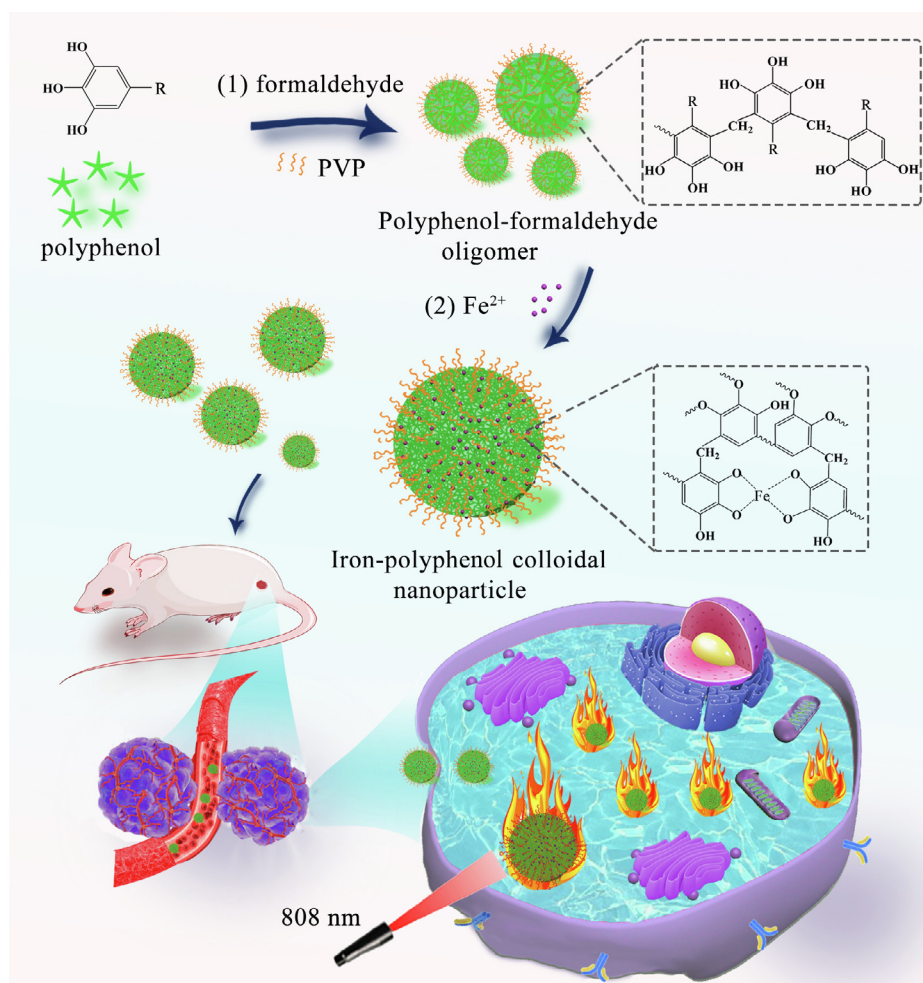
Tannic acid (TA, 98%), gallic acid (GA, 99%), epigallocatechin gallate (EGCG, 95%), epicatechin (EC, 95%), proanthocyanidin (PAC, 98%), FeSO<sub>4</sub>·7H<sub>2</sub>O (99%) and polyvinylpyrrolidone (PVP, M<sub>w</sub> = 58 kg/mol, 99%) were bought from Macklin Biochemical Co., Ltd. Formaldehyde solution (37 wt%) and ammonia solution (25 wt%) were bought from Tianjin Zhiyuan Chemical Co., Ltd. Calcein acetoxyethyl ester (Calcein-AM, 96%), propidium iodide (PI, 99%), 3-(4, 5-dimethylthiazol-2-yl)-2, 5-diphenyl-tetrazolium bromide (MTT, 97%) as well as Dulbecco's modified Eagle's medium (DMEM) were provided by Sigma-Aldrich Co. All the chemicals were employed in a direct way without further purification.

### 2.2. Synthesis of iron-polyphenol colloidal nanoparticles

The iron-polyphenol colloidal nanoparticles were synthesized via a sol-gel process based on different polyphenols as a ligand, including TA, EGCG, GA, EC and PAC. Typically, PVP (0.3 g) was dissolved in the mixture of water (37 mL), ethanol (8 mL) as well as ammonia (0.45 mL, 25 wt%). Subsequently, TA (0.2 g) was dissolved in the above solution followed by addition of formaldehyde solution (0.38 mL, 37 wt%). After 12 h, FeSO<sub>4</sub> aqueous solution (2 mL, 50 mg mL<sup>-1</sup>) was supplemented. After another 12 h, the solution was transferred to autoclave for hydrothermal treatment at 100 °C for 12 h. The obtained products were dialyzed to remove the small molecules (e.g., NH<sub>4</sub>OH). The solid products were collected via a freeze-dried process. When EGCG, GA, EC and PAC were used as an organic ligand, the synthesis procedure was similar. The amount of all the polyphenols kept 0.2 g. The obtained iron-polyphenol colloidal nanoparticles were denoted Fe-TA, Fe-EGCG, Fe-GA, Fe-EC and Fe-PAC, respectively.

### 2.3. Characterizations

Transmission electron microscopy (TEM) and scanning electron microscopy (SEM) images could be captured using JEM-F200 and Gemini SEM500, respectively. Inductively coupled plasma mass spectrometry (ICP-MS, NexION 350D) had been used for determining iron contents. Dynamic light scattering (DLS) and zeta potentials could be measured with Zetasizer Nano ZS (Malvern Instruments Ltd, UK). NIR lasers (808 nm, VCL-808, Beijinghonglan Laser) were adopted for NIR irradiation. Infrared images were collected by an infrared camera (FLIR, E8).



**Scheme 1.** Schematic illustration of the synthesis and PTT applications for iron-polyphenol colloidal nanoparticles.

#### 2.4. Photothermal performance

Iron-polyphenol colloidal solution at varying concentrations (0, 0.25, 0.5, 0.75, 1, and 1.5 mg/mL) should be under NIR laser irradiation (808 nm, 1.0–2.0 W/cm<sup>2</sup>) for 10 min. The real-time temperature and infrared images were collected using an infrared camera. Photothermal conversion efficiency ( $\eta$ ) could be measured in accordance with the previous report [46].

#### 2.5. *In vitro* cytotoxicity

Iron-polyphenol colloidal nanoparticles' cytotoxicity could be measured using MTT assay. Hela cell was used as a model [46]. To evaluate PTT performance, cells should be under laser exposure (1.0 W/cm<sup>2</sup>) for 5 min. Other procedures were same as that in the evaluation of cytotoxicity. The therapeutic effects were further evaluated by live/dead cell staining assays. Cells needed to be dyed in Calcein-AM (20 nM) and PI (100 nM) solution for 30 min. Finally, confocal laser scanning microscope was used to image the cells.

#### 2.6. *In vivo* photothermal therapy

EMT-6 tumour bearing BALB/C mice (20 g, female) were used as a model to evaluate photothermal therapy performance *in vivo*. Animal experiments followed The Care and Use of Laboratory

Animals of the Medical Research Council of Xi'an Jiaotong University. The mice bearing a 50 ~ 80 mm<sup>3</sup> EMT-6 tumour came under four groups ( $n = 5$ ) at random: PBS only (PBS group), Fe-TA only (Fe-TA group), PBS and NIR laser (Laser group), Fe-TA plus NIR laser (Fe-TA + Laser group). For Fe-TA + Laser group, the mice had intravenous injection of Fe-TA solution (4 mg/kg). Mouse tumors should be exposed to laser (808 nm, 1.0 W/cm<sup>2</sup>) for 5 min after injection for 4 h. During the treatment process, body weights and the tumour volumes were monitored every 2 day. On 18th day, all the mice were euthanized. The tumour tissues were weighted after resection. Meanwhile, prime mice organs like heart, spleen, liver, lung, kidney as well as tumour had been removed and preserved in 4% paraformaldehyde solution for histological analysis.

#### 2.7. *In vivo* biodistribution and clearance

The BALB/C mice ( $n = 3$ , 20 g, female) were sacrificed after 4, 12 and 72 h of intravenous injection with iron-polyphenol nanoparticles (4 mg/kg). Then, the main organs and tumour tissues were collected. After weighting, they were homogenized in cold PBS (1:2, w/v). The iron contents were measured by ICP-MS. To study the metabolic pathway of iron-polyphenol nanoparticles, three BALB/C mice (20 g, female) were intravenously injected with iron-polyphenol colloidal solution. The iron contents in urine and feces were determined by ICP-MS.

### 3. Results and discussion

Iron-polyphenol colloidal nanoparticles were synthesized via a modified sol-gel process based on our previous report [34]. Different kinds of polyphenols including TA, EGCG, GA, EC and PAC were selected as an organic ligand.  $\text{FeSO}_4 \cdot 7\text{H}_2\text{O}$  was used as an iron source. Polyphenols reacted with formaldehyde under the catalysis of ammonia hydroxide in the water/ethanol system. The polyphenol-formaldehyde oligomers were obtained with the assistance of PVP ( $M_w = 58 \text{ kg/mol}$ ). Then  $\text{Fe(II)}$  ions were added to chelate with the polyphenol-formaldehyde oligomers through metal-catchol coordination interactions. In the synthesis process, PVP was used to regulate the formation of iron-polyphenol nanoparticles and prevent them from aggregation. Consequently, iron-polyphenol colloidal nanoparticles with ultrasmall size and excellent colloidal stability were successfully obtained. They were denoted Fe-TA, Fe-EGCG, Fe-GA, Fe-EC and Fe-PAC, respectively.

The hydrodynamic diameter for iron-polyphenol colloidal nanoparticles was measured by DLS (Fig. 1a–e). The hydrodynamic diameter for Fe-TA, Fe-EGCG, Fe-GA, Fe-EC and Fe-PAC was 24, 21, 25, 27 and 30 nm, respectively. All the iron-polyphenol colloidal nanoparticles were highly dispersed in water with dark colour. The dark colour was associated with phenolic oxygen's

ligand-to-metal charge transfer band [44,55]. The UV-Vis-NIR absorption spectrum of five iron-polyphenol nanoparticles at the same concentration (1 mg/mL) was recorded (Fig. 1f). The absorbance of Fe-TA, Fe-EGCG, Fe-GA, Fe-EC and Fe-PAC at 808 nm was 0.705, 0.610, 0.440, 0.438 and 0.402, respectively. Their photothermal performance was further investigated. The iron-polyphenol colloidal solution with identical concentration (1 mg/mL) was under laser irradiation (808 nm,  $1.5 \text{ W/cm}^2$ ) for 10 min. Temperature of iron-polyphenol colloidal solution increased when irradiation time increased (Fig. 1g). Specifically, the temperature of Fe-TA, Fe-EGCG, Fe-GA, Fe-EC and Fe-PAC solution was 65.3, 58.6, 54.1, 48.5 and 46.5 °C after irradiation for 10 min (Fig. 1h). The photothermal conversion efficiency of Fe-TA, Fe-EGCG, Fe-GA, Fe-EC and Fe-PAC was around 43.6%, 37.9%, 36.1%, 35.8% and 35.2% according to the fitting cooling curve (Fig. 1i, Fig. S1). The photothermal conversion efficiency of such iron-polyphenol colloidal nanoparticles was comparable to that for other iron-polyphenol polymers with excellent photothermal performance (Table S1). The surface property of iron-polyphenol colloidal nanoparticles was also investigated. The zeta potentials of Fe-TA, Fe-EGCG, Fe-GA, Fe-EC and Fe-PAC were  $-4$ ,  $-4$ ,  $-3$ ,  $-5$  and  $-4 \text{ mV}$ , respectively (Fig. S2a). The zeta potentials of iron-polyphenol nanoparticles were depended on the amount of PVP polymers (Fig. S2b). In

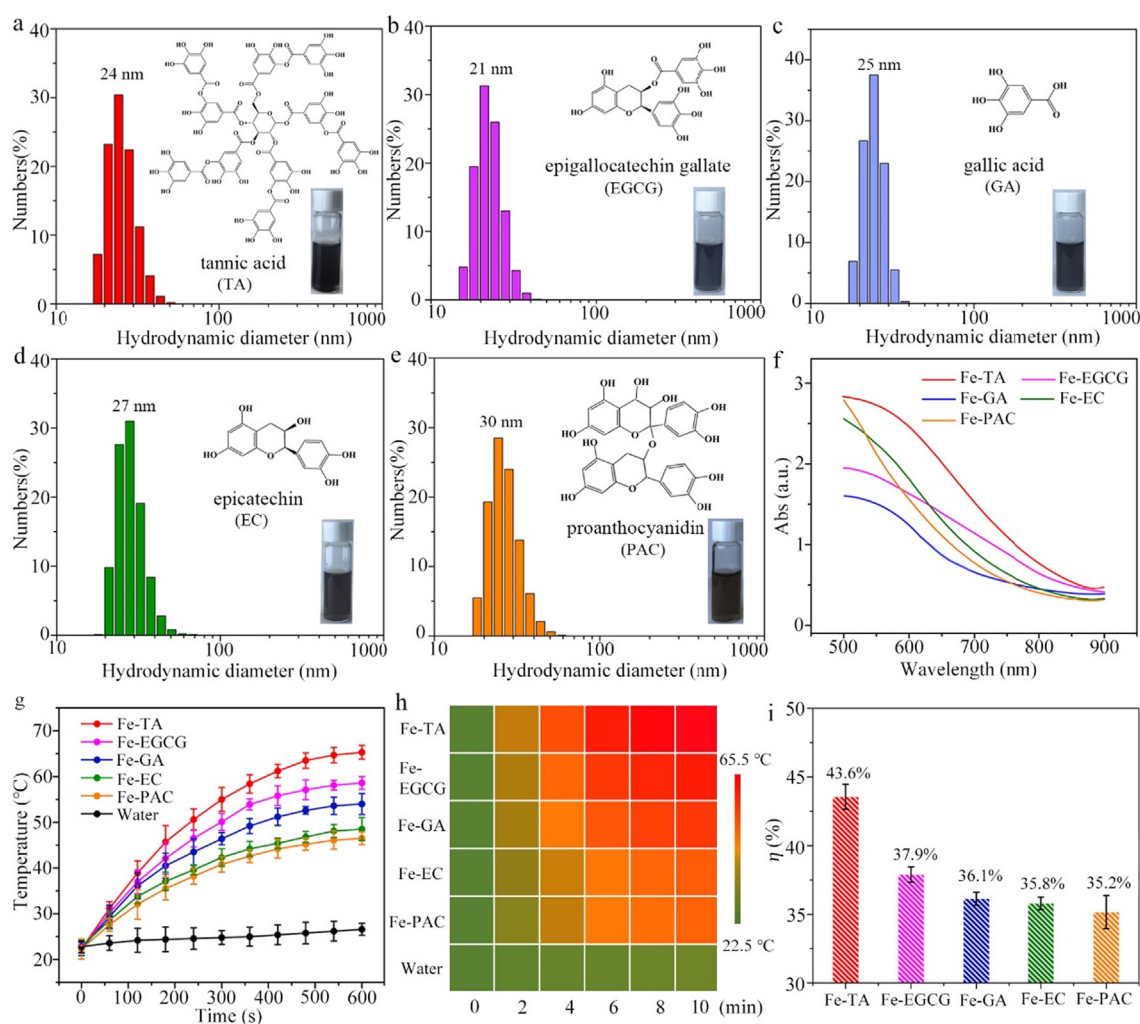


**Fig. 1.** The hydrodynamic size distributions of iron-polyphenol colloidal nanoparticles in water: (a) Fe-TA, (b) Fe-EGCG, (c) Fe-GA, (d) Fe-EC and (e) Fe-PAC. The inset is the corresponding photographs of iron-polyphenol nanoparticles in aqueous solution and chemical structures of polyphenols. (f) UV-Vis-NIR absorption spectrum of Fe-TA, Fe-EGCG, Fe-GA, Fe-EC and Fe-PAC solution (1.0 mg/mL). (g) Temperature change curves and (h) heat map of Fe-TA, Fe-EGCG, Fe-GA, Fe-EC and Fe-PAC solution (1.0 mg/mL) under laser irradiation (808 nm,  $1.5 \text{ W/cm}^2$ ). (i) Photothermal conversion efficiency of Fe-TA, Fe-EGCG, Fe-GA, Fe-EC and Fe-PAC. Results are presented as mean  $\pm$  S.D. ( $n = 3$ ).



case that PVP increased from 0 to 0.4 g, zeta potentials of Fe-TA nanoparticles changed from  $-21$  to  $-1$  mV. Such results revealed that the surface of nanoparticles was coated with nonionic PVP polymers.

To understand the relationship between composition and photothermal performance of iron-polyphenol colloidal nanoparticles, the iron contents were measured by ICP-MS (Fig. S3). The iron contents in Fe-TA, Fe-EGCG, Fe-GA, Fe-EC and Fe-PAC were 85.7, 72.3, 69.2, 65.4 and 60.3 mg/g, respectively. Iron content in Fe-TA was the highest among the iron-polyphenol nanoparticles. TA molecule has numerous catechol groups, which can coordinate with large amount of iron ions under alkaline condition. The photothermal performance was concerned with PTAs photo adsorption capability. The photo adsorption ability for iron-polyphenol colloidal nanoparticles was ascribed to the strong ligand-to-metal transfer properties. Therefore, the contents of iron species in the nanoparticles played a key role in enhancing the photothermal performance. A higher iron content results in a higher light adsorption and photothermal performance. To further verify the effects of iron content on the photothermal performance, Fe-TA colloidal nanoparticles with different iron contents were prepared by simply altering the proportion between iron precursor and tannic acid. The iron content in Fe-TA colloidal nanoparticles increased from 9.2 to 97.6 mg/g when the amount of metal precursor increased from 0.01 to 0.12 g (the amount of TA kept constant, 0.20 g, Fig. 2a). The sample was denoted Fe( $x$ )-TA ( $x = 0.01, 0.03, 0.05, 0.07, 0.1$  and  $0.12$ ,  $x$  referred the amount of iron precursor). The temperature of Fe( $x$ )-TA solution with the same concentration

(1 mg/mL) was recorded after irradiation for 10 min. The final temperature in Fe( $x$ )-TA solution enhanced when the content of Fe increased (Fig. 2b). When Fe content in Fe-TA was 14.3 mg/g, the final temperature of solution was as low as  $32^\circ\text{C}$  after irradiation for 10 min. When Fe content in Fe-TA was 85.7 mg/g, the temperature of Fe-TA solution was  $65.3^\circ\text{C}$ . When Fe content in Fe-TA was 97.6 mg/g, the temperature of Fe-TA solution was  $55^\circ\text{C}$ . The decreased temperature may be ascribed to the limited chelating capacity of polyphenols. When excess Fe precursors were added, Fe-TA nanoparticles tended to agglomerate (Fig. S4). The excess Fe ions would act as a crosslinker to bind the adjacent colloidal nanoparticles, resulting in the agglomeration of iron-polyphenol nanoparticles. The photothermal performance of iron-polyphenol colloidal nanoparticles was closely related to the iron content. Higher iron content in the colloidal nanoparticles resulted into higher photothermal performance. The excess iron species led to the agglomeration of iron-polyphenol nanoparticles and lowered the photothermal performance.

The effect of particle size on the photothermal performance was investigated. The amount of PVP was changed during the synthesis process while keeping the ratio of iron/TA unchanged. Fe-TA nanoparticles with different size were obtained (Fig. 2c). The hydrodynamic size of Fe-TA nanoparticles was 24, 77, 164, 269 and 303 nm, respectively. The size of Fe-TA nanoparticles decreased dramatically with the increase of PVP. PVP polymers attached onto the surface of Fe-TA nanoparticles and prevented the agglomeration of nanoparticles. The photothermal performance for Fe-TA nanoparticles with different size was then

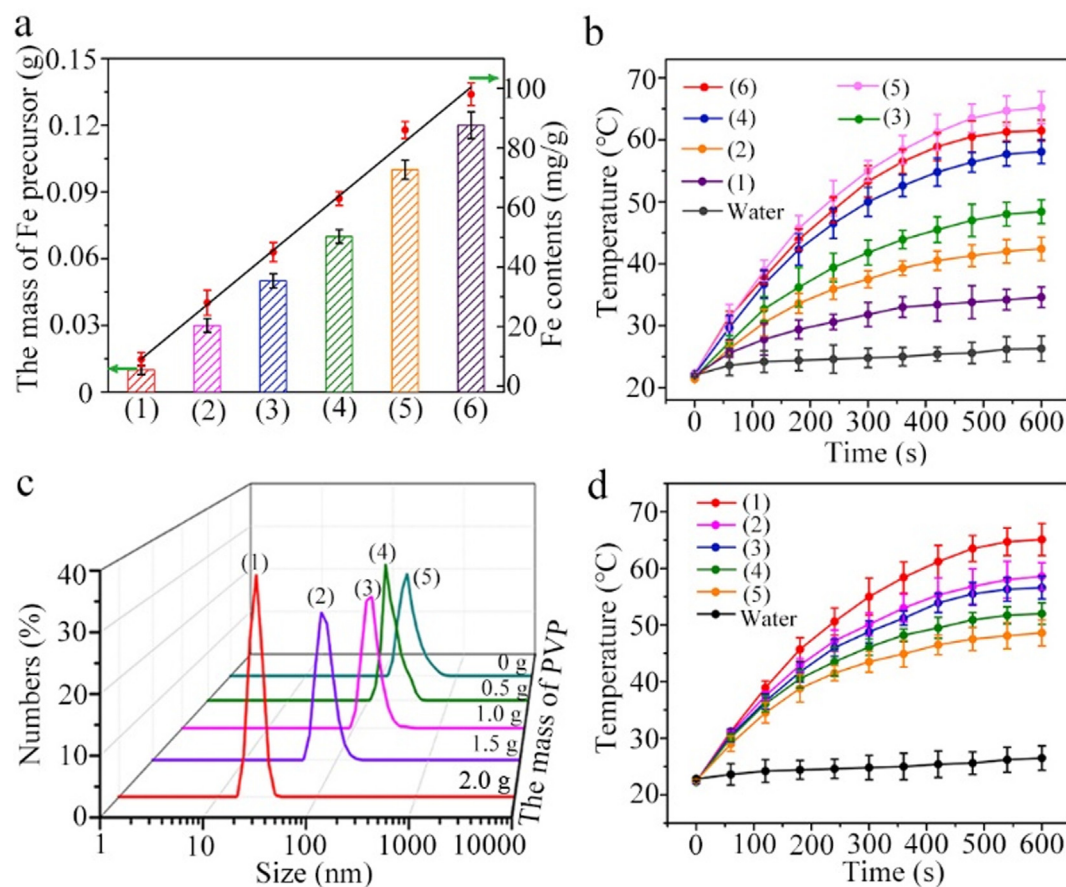


**Fig. 2.** (a) The mass of metal precursors versus the contents of Fe in Fe( $x$ )-TA nanoparticles. (b) Photothermal curves of Fe( $x$ )-TA with different contents of Fe under laser (808 nm, 1.5 W/cm<sup>2</sup>). (1)–(6) in Fig. 2a and b were Fe(0.01)-TA, Fe(0.03)-TA, Fe(0.05)-TA, Fe(0.07)-TA, Fe(0.1)-TA and Fe(0.12)-TA, respectively. (c) The hydrodynamic size of Fe-TA synthesized using varying amount of PVP. The size of (1)–(5) was 24, 77, 164, 269 and 303 nm, respectively. (d) Photothermal curves of Fe-TA with different size. (1)–(5) referred Fe-TA with different size (24, 77, 164, 269 and 303 nm). Findings should be presented as mean  $\pm$  S.D. ( $n = 3$ ).

investigated. The final temperature of Fe-TA colloidal solution increased when the size of Fe-TA decreased (Fig. 2d). When the size of nanoparticles become smaller, the nanoparticles showed higher absorption/scattering ratios [56–58]. Therefore, more light energy can be converted to heat energy. The final temperature of Fe-TA solution increased when the size of Fe-TA decreased (Fig. 2d). The above results indicated that the photothermal performance of Fe-TA was related to the particle size.

Based on the above results, Fe-TA colloidal nanoparticles with hydrodynamic size of 24 nm were selected as a typical photothermal agent for further investigation. Fe-TA colloidal solution showed no precipitation for 30 days. The hydrodynamic diameter kept nearly constant (26 nm), indicating high colloidal stability (Fig. 3a). TEM image of Fe-TA nanoparticles was spherical, and its mean diameter was around 20 nm (Fig. 3b). The atomic force microscopy (AFM) image also confirmed this result (Fig. 3c-d). Furthermore, Fe-TA nanoparticles exhibited excellent hydrophilicity and stability in different dispersants, including water, phosphate-buffer saline (PBS), 0.9% NaCl solution, Tris-Borate-EDTA (TBE) and Dulbecco's modified Eagle medium (DMEM). The hydrodynamic size of Fe-TA in HEPES, TBE, PBS, NaCl, Tris-HCl and DMEM buffers was 30, 28, 22, 27, 25 and 20 nm, respectively (Fig. S5a, b). Such good dispersibility in different buffers is beneficial to their biomedical applications.

The impact by concentration and power density on photothermal performance was studied. Fe-TA colloidal solution (diameter: 24 nm) with different concentrations (0–1.5 mg/mL) was exposed to laser (1.5 W/cm<sup>2</sup>). The temperature of the solution increased

rapidly when the irradiation time increased from 0 to 10 min (Fig. 4a). Thermographic images of Fe-TA colloidal solution with different concentrations further proved excellent photothermal performance (Fig. 4b). The temperature of Fe-TA colloidal solution (1.0 mg/mL) increased to 65.3 °C under laser irradiation (1.5 W / cm<sup>2</sup>). The final temperature in Fe-TA colloidal solution was related to the power density of laser (Fig. 4c). Both the equilibrium temperature and the absorption at 808 nm of Fe-TA solution were nearly unchanged after four cycles of irradiation (Fig. 4d, Fig. S6), indicating a high photostability of Fe-TA colloidal solution.

Encouraged by the excellent photothermal performance of iron-polyphenol colloidal nanoparticles, we further investigated their cytotoxicity and *in vitro* PTT performance. The cytotoxicity was evaluated through MTT assay using Hela as a model cell. The cytotoxicity of Fe-TA was relatively low without NIR irradiation (Fig. 4e). The cell viability remained approximately 90.1% when Fe-TA colloidal solution concentration reached to 1.0 mg/mL. Comparably, Fe-TA colloidal nanoparticles showed an obvious inhibition effect on cell viability under NIR irradiation. As Fe-TA colloidal solution concentration increased, the cell viability under NIR irradiation decreased obviously. 23.0% of Hela cells survived when Fe-TA colloidal solution concentration approached 1.0 mg/mL under NIR irradiation. These findings demonstrated that Fe-TA had a great potential as a photothermal agent of PTT. Hela cells could be considered model tumour cells and received different treatments: control (Group I), Fe-TA only (Group II), 808 nm laser irradiation only (Group III), and Fe-TA plus 808 nm laser irradiation (Group IV). Processed cells could be co-stained with Calcein-AM as

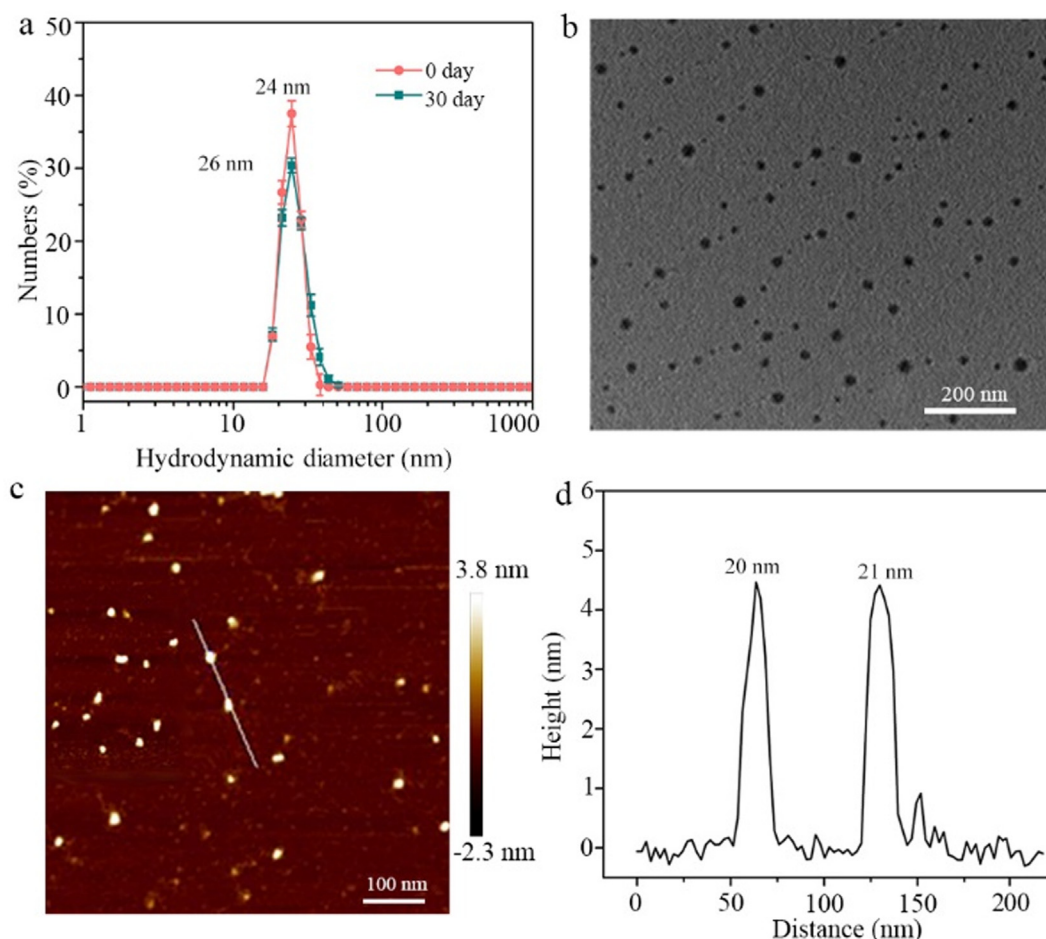


**Fig. 3.** (a) Hydrodynamic diameter for Fe-TA on 0 and 30 day. Findings have been expressed by mean  $\pm$  S.D. ( $n = 3$ ). (b) TEM and (c) AFM image for Fe-TA. (d) The height profile along the line labeled in AFM image.

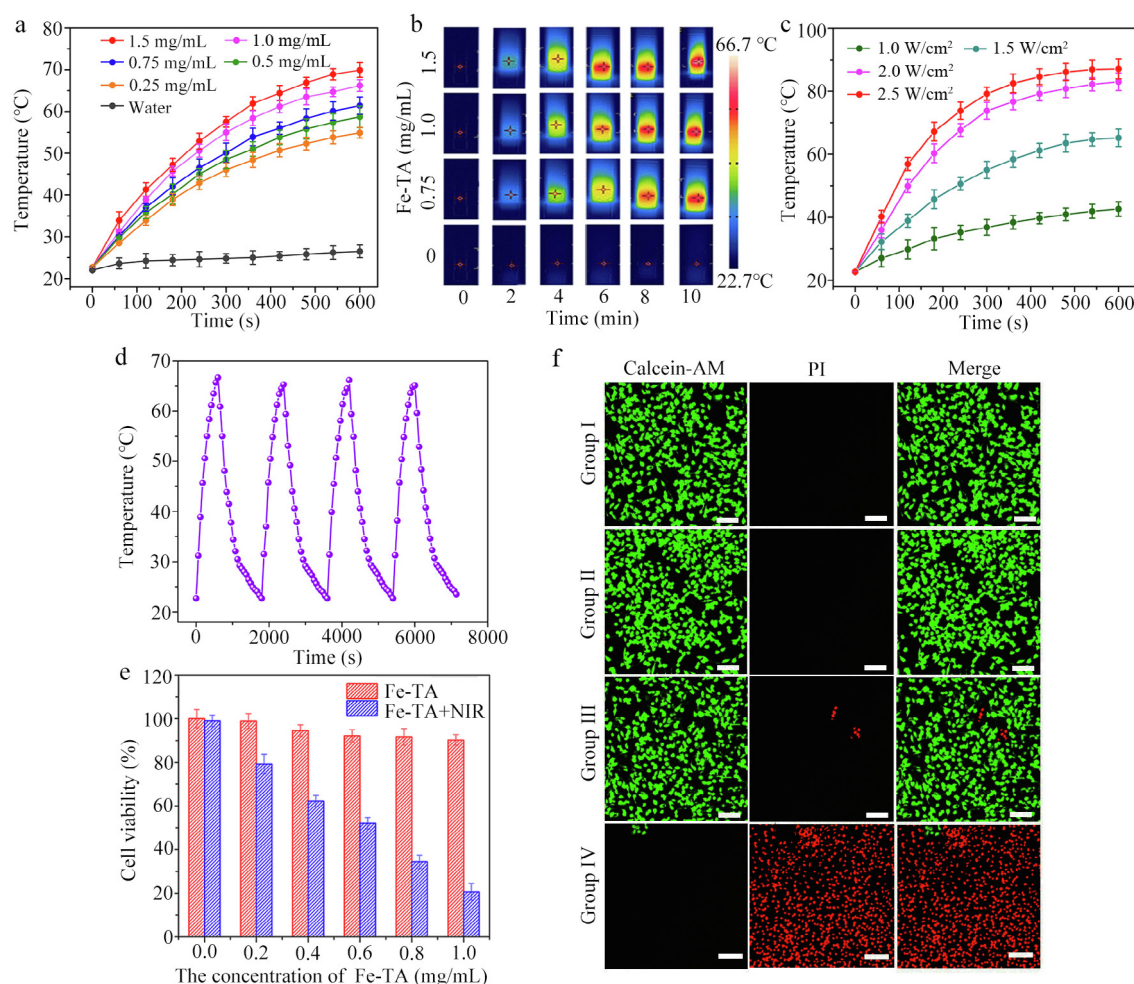


**Fig. 4.** (a) Time-dependent temperature change curves for Fe-TA solution at each concentration under laser irradiation (808 nm, 1.5 W/cm<sup>2</sup>). (b) Thermographic images of Fe-TA solution with different concentrations (0–1.5 mg/mL) under a laser (808 nm, 1.5 W/cm<sup>2</sup>) for 0–10 min. (c) Temperature elevation curves for Fe-TA over four cycles (ON/OFF) of laser. (d) Power-dependent temperature change curves of Fe-TA solution with 1 mg/mL under laser irradiation (808 nm) with varying power density. (e) The HeLa cell viability after incubation using Fe-TA with varying concentrations with (or without) laser exposure (808 nm, 1.0 W/cm<sup>2</sup>) for 5 min. (f) Confocal fluorescence images for calcein AM (green) and PI (red) containing HeLa cells following various processing. Scale bar, 100  $\mu$ m. Findings should be expressed by mean  $\pm$  S.D. ( $n = 3$ ). (For interpretation of the references to colour in this figure legend, the reader is referred to the web version of this article.)

well as PI. Negligible cell death was observed in Group I, II and III. Comparably, almost all the cells were killed in Group IV (Fig. 4f). The obtained results indicated that Fe-TA colloidal nanoparticles had low cytotoxicity. However, Fe-TA colloidal nanoparticles efficiently killed cancer cell with the assistance of laser via the photothermal process.

Based on the efficient photothermal performance of Fe-TA *in vitro*, we further evaluated the therapeutic effect using BALB/C mice bearing EMT-6 tumour as a model. All animal experiments were carried out based on The Care and Use of Laboratory Animals of the Medical Research Council in Xi'an Jiaotong University. After intravenously injection of Fe-TA colloidal solution for 4 h, the mice were exposed to a laser (808 nm, 1.5 W/cm<sup>2</sup>) for 5 min. The spatial distributions of temperature at the tumour site were monitored with an infrared imaging camera. The temperature of the tumour region with injection of Fe-TA dramatically increased from 34 to 57 °C within 5 min. By comparison, the temperature of the tumour region for the control group (injection of PBS only) increased from 34 to 40 °C (Fig. 5a, b). Such results revealed the excellent photothermal performance of Fe-TA *in vivo*, making it possible to eliminate tumours of mice.

The mice came under four groups ( $n = 5$ ) randomly, including phosphate buffer saline (control group), Fe-TA nanoparticles only

(Fe-TA group), 808 nm NIR laser only (Laser group), and Fe-TA nanoparticles plus 808 nm NIR laser (Fe-TA + Laser group). The body weight was within a normal range for all groups during the treatment process, indicating a low systemic toxicity of Fe-TA (Fig. 5c). The tumour growth rate and final size for Fe-TA group and Laser group were similar to those of the control group, suggesting that laser irradiation or Fe-TA alone would not effectively inhibit the tumour growth (Fig. 5d). It should be noted that the volume of tumour in the Fe-TA + Laser group was much smaller compared with that in the control group, indicating successful photothermal ablation of the tumours (Fig. 5e, Fig. S7). Furthermore, the histological analysis of tumours confirmed that tumour cells experienced serious damages in Fe-TA + Laser group (Fig. 5f).

To evaluate the biodistribution of Fe-TA in mice, tumour-bearing mice were sacrificed at 0, 4, 12 and 72 h after injection of iron-polyphenol colloidal solution. Iron contents in main organs (spleen, heart, kidney, liver, lung) and tumour were measured via ICP-MS. The iron content reached highest in tumour after 4 h of injection (Fig. S8a). Fe-TA nanoparticles could effectively accumulate in the tumour region due to the enhanced permeability and retention effects. The iron content of liver also revealed a peak after 4 h of injection, indicating that Fe-TA nanoparticles were mainly captured by the reticuloendothelial system. Four hours later, liver



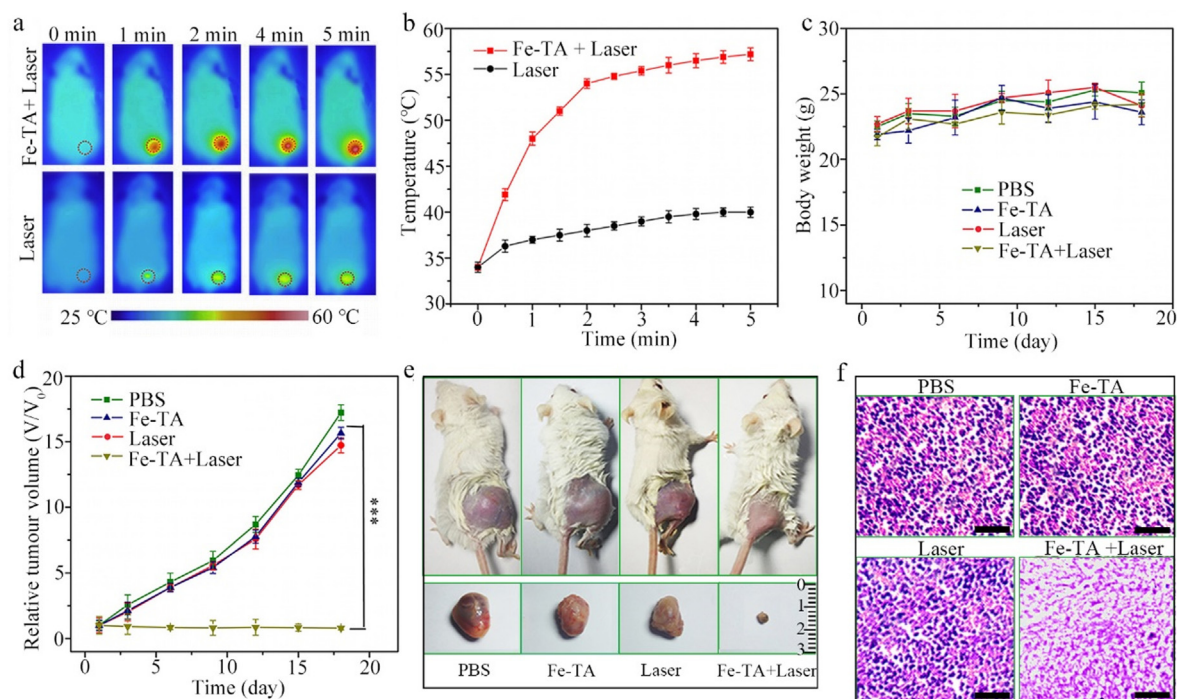


**Fig. 5.** (a) *In vivo* infrared thermal images for mice following intravenous injection with or without Fe-TA under laser irradiation (1.5 W/cm<sup>2</sup>, 5 min). (b) Temperature in tumour region versus irradiation time. (c) Body weight and (d) tumour volume curves of different groups of mice. (e) Photograph for mice and tumour harvested following different treatments after 18 days. (f) H&E staining of tumour slides. Findings should be expressed by mean  $\pm$  S.D. ( $n = 5$ , \* $p < 0.05$ , \*\* $p < 0.01$ , \*\*\* $p < 0.001$ , measured using Student's *t*-test). Scale bar: 50  $\mu$ m.

iron content progressively lowered and recovered after 72 h. *In vivo* metabolic pathway of Fe-TA nanoparticles was further investigated (Fig. S8b). The iron content in urine and feces of mice at different time intervals was measured by ICP-MS. There were 61.1% and 35.5% of Fe-TA eliminated through feces and urine after 60 h. Such results revealed that Fe-TA nanoparticles were smoothly discharged from mouse body through hepatobiliary pathway [59,60].

Lastly, *in vivo* toxicity of Fe-TA colloidal nanoparticles was investigated by hematological and histochemical analysis. For the hematological assessment, the blood parameters associated with acute toxicity were normal except for the white blood cell (WBC) count (Fig. S9) [61]. The WBC level after injection with Fe-TA solution was lower in comparison with that of the control group after 1 day of injection. However, WBC level recovered after 3 days. The temporal decrease of WBC level could be ascribed to body temporal iron overload [62]. The WBC level recovered to a normal range when Fe-TA nanoparticles were cleared. The main organ like heart, liver, spleen, lung and kidney should be extracted in histology analysis on day 1 and 3 after injection of Fe-TA solution. In comparison with the normal mice, neither noticeable inflammation nor damage was observed in the major organ (Fig. S10). These results indicated that Fe-TA nanoparticles showed low toxicity to the mice with the current experimental dosage.

#### 4. Conclusion

A general strategy is demonstrated to synthesize iron-polyphenol colloidal nanoparticles with tunable diameter (21–303 nm) and iron content (9.2–97.6 mg/g), as well as high colloidal stability using different polyphenols (such as tannic acid, epigallocatechin gallate, gallic acid, epicatechin and proanthocyanidin) as an organic ligand. The photothermal performance of such nanoparticles depends on the kind of polyphenol ligand, iron content and particle size. Generally, iron-tannic acid colloidal nanoparticles

with high iron contents and small particle size show high photothermal performance. To inhibit tumour growth *in vivo*, the iron-polyphenol colloidal nanoparticles are further used as an efficient photothermal agent. To date, most of reported iron-polyphenol colloidal nanoparticles show uncontrollable particle size and monotonous ligand [44–45]. Besides, the current work provides a versatile strategy for rational design and synthesis of polyphenol-based colloids with tunable diameter and compositions. Moreover, the relationship between material composition and photothermal performance is systematically investigated. The current work is conducive to rational design of polyphenol-based photothermal agent. Based on the proposed synthesis strategy, other plant polyphenols could also be used to fabricate polyphenol-based colloidal nanoparticles with special property or function. We believe that functional polyphenol-based colloidal nanoparticles would exhibit promising prospects for biomedical imaging and cancer treatment.

#### CRediT authorship contribution statement

**Jing Qin:** Investigation, Formal analysis, Writing - original draft. **Guohai Liang:** Investigation, Data curation, Writing - original draft, Funding acquisition. **Dong Cheng:** Investigation, Data curation, Writing - original draft. **Yining Liu:** Investigation, Data curation. **Xiaoran Cheng:** Investigation, Data curation. **Pengkun Yang:** Investigation, Data curation. **Na Wu:** Investigation, Data curation. **Yongxi Zhao:** Supervision, Writing - review & editing. **Jing Wei:** Supervision, Writing - review & editing, Funding acquisition.

#### Declaration of Competing Interest

The authors declare that they have no known competing financial interests or personal relationships that could have appeared to influence the work reported in this paper.



## Acknowledgements

The current research gained sponsorship from the National Natural Science Foundation of China (No. 21701130 and 311343). We feel appreciated for Mr Zijun Ren from Instrument Analysis Center in Xi'an Jiaotong University for his help in TEM and SEM analysis.

## Appendix A. Supplementary material

Supplementary data to this article can be found online at <https://doi.org/10.1016/j.jcis.2021.02.082>.

## References

- [1] M. Li, X. Yang, J. Ren, K. Qu, X. Qu, Using graphene oxide high near-infrared absorbance for photothermal treatment of alzheimer's disease, *Adv. Mater.* 24 (13) (2012) 1722–1728.
- [2] Q. Chen, L. Xu, C. Liang, C. Wang, R. Peng, Z. Liu, Photothermal therapy with immune-adjuvant nanoparticles together with checkpoint blockade for effective cancer immunotherapy, *Nat. Commun.* 7 (2016) 13193.
- [3] S. Wang, P. Huang, L. Nie, R. Xing, D. Liu, Z. Wang, J. Lin, S. Chen, G. Niu, G. Lu, X. Chen, Single continuous wave laser induced photodynamic/plasmonic photothermal therapy using photosensitizer-functionalized gold nanostars, *Adv. Mater.* 25 (22) (2013) 3055–3061.
- [4] S. Lal, S.E. Clare, N.J. Halas, Nanoshell-enabled photothermal cancer therapy: impending clinical impact, *Acc. Chem. Res.* 41 (12) (2008) 1842–1851.
- [5] Y. Liu, P. Bhattarai, Z. Dai, X. Chen, Photothermal therapy and photoacoustic imaging via nanotheranostics in fighting cancer, *Chem. Soc. Rev.* 48 (7) (2019) 2053–2108.
- [6] C.M. Cobley, J.Y. Chen, E.C. Cho, L.V. Wang, Y.N. Xia, Gold nanostructures: a class of multifunctional materials for biomedical applications, *Chem. Soc. Rev.* 40 (2011) 44–56.
- [7] W. Fang, S. Tang, P. Liu, X. Fang, J. Gong, N. Zheng, Pd nanosheet-covered hollow mesoporous silica nanoparticles as a platform for the chemophotothermal treatment of cancer cells, *Small* 8 (24) (2012) 3816–3822.
- [8] D.D. Wang, Z. Guo, J.J. Zhou, J. Chen, G.Z. Zhao, R.H. Chen, M.N. He, Z.B. Liu, H.B. Wang, Q.W. Chen, Novel  $\text{Mn}_3[\text{Co}(\text{CN})_6]_2/\text{SiO}_2/\text{Ag}$  core-shell nanocube: enhanced two photon fluorescence and magnetic resonance dual-modal imaging guided photothermal and chemo-therapy, *Small* 11 (2015) 5956–5967.
- [9] H.K. Moon, S.H. Lee, H.C. Choi, In vivo near-infrared mediated tumour destruction by photothermal effect of carbon nanotubes, *ACS Nano* 3 (2009) 3707–3713.
- [10] K. Yang, S. Zhang, G.X. Zhang, X.M. Sun, S.T. Lee, Z.A. Liu, Graphene in mice: ultrahigh in vivo tumour uptake and efficient photothermal therapy, *Nano Lett.* 10 (2010) 3318–3323.
- [11] H. Wang, Y. Sun, J. Yi, J. Fu, J. Di, A. del Carmen Alonso, S. Zhou, Fluorescent porous carbon nanocapsules for two-photon imaging, NIR/pH dual-responsive drug carrier, and photothermal therapy, *Biomaterials* 53 (2015) 117–126.
- [12] B. Liu, C.X. Li, B.G. Xing, P.P. Yang, J. Lin, Multifunctional UCNP@PDA-ICG nanocomposites for upconversion imaging and combined photothermal/photodynamic therapy with enhanced antitumour efficacy, *J. Mater. Chem. B* 4 (2016) 4884–4894.
- [13] J. Yang, J. Choi, D. Bang, E. Kim, E.-K. Lim, H. Park, J.-S. Suh, K. Lee, K.-H. Yoo, E.-K. Kim, Y.-M. Huh, S. Haam, Convertible organic nanoparticles for near-infrared photothermal ablation of cancer cells, *Angew. Chem. Int. Ed.* 50 (2) (2011) 441–444.
- [14] S.S. Chou, B. Kaehr, J. Kim, B.M. Foley, M. De, P.E. Hopkins, J. Huang, C.J. Brinker, V.P. Dravid, Chemically exfoliated  $\text{MoS}_2$  as near-infrared photothermal agents, *Angew. Chem. Int. Ed.* 52 (15) (2013) 4160–4164.
- [15] L. Cheng, J. Liu, X. Gu, H. Gong, X. Shi, T. Liu, C. Wang, X. Wang, G. Liu, H. Xing, W. Bu, B. Sun, Z. Liu, PEGylated  $\text{WS}_2$  nanosheets as a multifunctional theranostic agent for in vivo dual-modal CT/photoacoustic imaging guided photothermal therapy, *Adv. Mater.* 26 (12) (2014) 1886–1893.
- [16] Y.u. Chen, L. Wang, J. Shi, Two-dimensional non-carbonaceous materials-enabled efficient photothermal cancer therapy, *Nano Today* 11 (3) (2016) 292–308.
- [17] L. Cheng, H. Gong, W. Zhu, J. Liu, X. Wang, G. Liu, Z. Liu, PEGylated prussian blue nanocubes as a theranostic agent for simultaneous cancer imaging and photothermal therapy, *Biomaterials* 35 (37) (2014) 9844–9852.
- [18] S. Sharifi, S. Behzadi, S. Laurent, M. Laird Forrest, P. Stroeve, M. Mahmoudi, Toxicity of nanomaterials, *Chem. Soc. Rev.* 41 (6) (2012) 2323–2343.
- [19] Y. Jiang, C. Huang, Y. Luan, Lactosylated IR820/DOX co-assembled nanodrug for synergistic antitumour therapy, *Int. J. Nanomed.* 15 (2020) 4431–4440.
- [20] H. Zhang, J. Zhang, Q. Li, A. Song, H. Tian, J. Wang, Z. Li, Y. Luan, Site-specific MOF-based immunotherapeutic nanoplateforms via synergistic tumor cells-targeted treatment and dendritic cells-targeted immunomodulation, *Biomaterials* 245 (2020) 119983.
- [21] L.Q. Xu, K.-G. Neoh, E.-T. Kang, Natural polyphenols as versatile platforms for material engineering and surface functionalization, *Prog. Polym. Sci.* 87 (2018) 165–196.
- [22] W. Zhu, J. Guo, Y. Ju, R.E. Serda, J.G. Croissant, J. Shang, E. Coker, J.O. Agola, Q.-Z. Zhong, Y. Ping, Modular metal-organic polyhedra superassembly: from molecular-level design to targeted drug delivery, *Adv. Mater.* 31 (2019) 1806774.
- [23] J. Cui, K. Alt, Y. Ju, S.T. Gunawan, J.A. Braunger, T.-Y. Wang, Y. Dai, Q. Dai, J.J. Richardson, J. Guo, Ligand functionalized Poly(ethylene glycol) particles for tumour targeting and intracellular uptake, *Biomacromolecules* 20 (2019) 3592–3600.
- [24] M.A. Rahim, S.L. Kristufek, S. Pan, J.J. Richardson, F. Caruso, Phenolic building blocks for the assembly of functional materials, *Angew. Chem. Int. Ed.* 58 (7) (2019) 1904–1927.
- [25] A. Shavandi, A.-D. Bekhit, P. Saeedi, Z. Izadifar, A.A. Bekhit, A. Khademhosseini, Polyphenol uses in biomaterials engineering, *Biomaterials* 167 (2018) 91–106.
- [26] S. Quideau, D. Deffieux, C. Douat-Casassus, L. Pouységu, Plant polyphenols: chemical properties, biological activities, and synthesis, *Angew. Chem. Int. Ed.* 50 (3) (2011) 586–621.
- [27] H. Ejima, J.J. Richardson, K. Liang, J.P. Best, M.P. van Koeveden, G.K. Such, J. Cui, F. Caruso, One-step assembly of coordination complexes for versatile film and particle engineering, *Science* 341 (2013) 154.
- [28] J. Guo, Y. Ping, H. Ejima, K. Alt, M. Meissner, J.J. Richardson, Y. Yan, K. Peter, D. von Elverfeldt, C.E. Hagemeyer, F. Caruso, Engineering multifunctional capsules through the assembly of metal-phenolic networks, *Angew. Chem. Int. Ed.* 53 (22) (2014) 5546–5551.
- [29] J. Wei, Y. Liang, Y. Hu, B. Kong, J. Zhang, Q. Gu, Y. Tong, X. Wang, S.P. Jiang, H. Wang, Hydrothermal synthesis of metal-polyphenol coordination crystals and their derived metal/N-doped carbon composites for oxygen electrocatalysis, *Angew. Chem. Int. Ed.* 55 (40) (2016) 12470–12474.
- [30] J. Wei, Y. Liang, Y. Hu, B. Kong, G. P. Simon, J. Zhang, S. P. Jiang, H. Wang, A. versatile iron-tannin-framework ink coating strategy to fabricate biomass-derived iron carbide/Fe-N-carbon catalysts for efficient oxygen reduction, *Angew. Chem. Int. Ed.* 55 (2016) 1355–1359.
- [31] C. Maerten, L. Lopez, P. Lupattelli, G. Rydzek, S. Pronkin, P. Schaaf, L. Jierry, F. Boulmedais, Electrotriggered confined self-assembly of metal-polyphenol nanocoatings using a morphogenic approach, *Chem. Mater.* 29 (2017) 9668–9679.
- [32] X. Chen, Z. Yi, G. Chen, X. Ma, W. Su, X. Cui, X. Li, DOX-assisted functionalization of green tea polyphenol nanoparticles for effective chemophotothermal cancer therapy, *J. Mater. Chem. B* 7 (2019) 4066–4078.
- [33] G. Wang, J. Qin, X. Zhou, Y. Deng, H. Wang, Y. Zhao, J. Wei, Self-template synthesis of mesoporous metal oxide spheres with metal-mediated inner architectures and superior sensing performance, *Adv. Funct. Mater.* 28 (2018) 1806144.
- [34] J. Wei, G. Wang, F. Chen, M. Bai, Y. Liang, H. Wang, D. Zhao, Y. Zhao, Sol-gel synthesis of metal-phenolic coordination spheres and their derived carbon composites, *Angew. Chem. Int. Ed.* 57 (2018) 9838–9843.
- [35] G. Wang, J. Qin, Y. Feng, B. Feng, S. Yang, Z. Wang, Y. Zhao, J. Wei, Sol-gel synthesis of spherical mesoporous high-entropy-oxides, *ACS Appl. Mater. Interfaces* 12 (2020) 45155–45164.
- [36] G. Wang, J. Qin, Y. Zhao, J. Wei, Nanoporous carbon spheres derived from metal-phenolic coordination polymers for supercapacitor and biosensor, *J. Colloid Interface Sci.* 544 (2019) 241–248.
- [37] G. Wang, X. Zhou, J. Qin, Y. Liang, B. Feng, Y. Deng, Y. Zhao, J. Wei, General Synthesis of mixed semiconducting metal oxide hollow spheres with tunable compositions for low-temperature chemiresistive sensing, *ACS Appl. Mater. Interfaces* 11 (38) (2019) 35060–35067.
- [38] X. Wei, D. Zheng, M. Zhao, H. Chen, X. Fan, B. Gao, L. Gu, Y. Guo, J. Qin, J. Wei, Y. Zhao, G. Zhang, Cross-linked polyphosphazene hollow nanosphere derived N/P doped porous carbon with single nonprecious metal atoms for oxygen reduction reaction, *Angew. Chem. Int. Ed.* 59 (2020) 14639–14646.
- [39] Z. Dong, L. Feng, Y. Chao, Y. Hao, M. Chen, F. Gong, X. Han, R. Zhang, L. Cheng, Z. Liu, Amplification of tumour oxidative stresses with liposomal Fenton catalyst and glutathione inhibitor for enhanced cancer chemotherapy and radiotherapy, *Nano Lett.* 19 (2019) 805–815.
- [40] Y. Dai, J. Guo, T.Y. Wang, Y. Ju, A.J. Mitchell, T. Bonnard, J. Cui, J.J. Richardson, C. E. Hagemeyer, K. Alt, F. Caruso, Self-assembled nanoparticles from phenolic derivatives for cancer therapy, *Adv. Healthcare Mater.* 6 (2017) 1700467.
- [41] Y. Dai, S. Cheng, Z. Wang, R. Zhang, Z. Yang, J. Wang, B.C. Yung, Z. Wang, O. Jacobson, C. Xu, Q. Ni, G. Yu, Z. Zhou, X. Chen, Hypochlorous acid promoted platinum drug chemotherapy by myeloperoxidase-encapsulated therapeutic metal phenolic nanoparticles, *ACS Nano* 12 (2018) 455–463.
- [42] C. Wang, H. Sang, Y. Wang, F. Zhu, X. Hu, X. Wang, X. Wang, Y. Li, Y. Cheng, Foe to friend: supramolecular nanomedicines consisting of natural polyphenols and bortezomib, *Nano Lett.* 18 (2018) 7045–7051.
- [43] W. Zhu, G. Xiang, J. Shang, J. Guo, B. Motevali, P. Durfee, J.O. Agola, E.N. Coker, C.J. Brinker, Versatile surface functionalization of metal-organic frameworks through direct metal coordination with a phenolic lipid enables diverse applications, *Adv. Funct. Mater.* 28 (2018) 1705274.
- [44] F. Liu, X. He, H. Chen, J. Zhang, H. Zhang, Z. Wang, Gram-scale synthesis of coordination polymer nanodots with renal clearance properties for cancer theranostic applications, *Nat. Commun.* 6 (2015) 8003.
- [45] G. Zhao, H. Wu, R. Peng, D. Wang, P. Xu, P. Jiang, K. Yang, H. Wang, Z. Guo, Q. Chen, Novel metal polyphenol framework for MR imaging-guided photothermal therapy, *ACS Appl. Mater. Interfaces* 10 (2018) 3295–3304.
- [46] J. Qin, G. Liang, Y. Feng, B. Feng, G. Wang, N. Wu, Y. Zhao, J. Wei, Synthesis of gadolinium/iron-bimetal-phenolic coordination polymer nanoparticles for theranostic applications, *Nanoscale* 12 (2020) 6096.

- [47] T. Liu, M. Zhang, W. Liu, X. Zeng, X. Song, X. Yang, X. Zhang, J. Feng, Metal ion/tannic acid assembly as a versatile photothermal platform in engineering multimodal nanotheranostics for advanced applications, *ACS Nano* 12 (2018) 3917–3927.
- [48] Y. Wang, J. Zhang, C. Zhang, B. Li, J. Wang, X. Zhang, D. Li, S.K. Sun, Functional-protein-assisted fabrication of Fe-gallic acid coordination polymer nanonetworks for localized photothermal therapy, *ACS Sustainable Chem. Eng.* 7 (2019) 994–1005.
- [49] P. Zhang, Y. Hou, J. Zeng, Y. Li, Z. Wang, R. Zhu, T. Ma, M. Gao, Coordinatively unsaturated  $\text{Fe}^{3+}$  based activatable probes for enhanced MRI and therapy of tumours, *Angew. Chem. Int. Ed.* 58 (2019) 11088–11096.
- [50] Y. Li, Y. Huang, Z. Wang, F. Carniato, Y. Xie, J.P. Patterson, M.P. Thompson, C.M. Andolina, T.B. Ditri, J.E. Millstone, J.S. Figueroa, J. Rinehart, M. Scadeng, M. Botta, N.C. Gianneschi, Polycatechol nanoparticle MRI contrast agents, *Small* 12 (2016) 668–677.
- [51] J. Zeng, M. Cheng, Y. Wang, L. Wen, L. Chen, Z. Li, Y. Wu, M. Gao, Z. Chai, pH-responsive  $\text{Fe(III)}$ -gallic acid nanoparticles for in vivo photoacoustic-imaging-guided photothermal therapy, *Adv. Healthcare Mater.* 5 (2016) 772–780.
- [52] Q. Jin, W. Zhu, D. Jiang, R. Zhang, C.J. Kutyreff, J.W. Engle, P. Huang, W. Cai, Z. Liu, L. Cheng, Ultra-small iron-gallic acid coordination polymer nanoparticles for chelator-free labeling of  $^{64}\text{Cu}$  and multimodal imaging-guided photothermal therapy, *Nanoscale* 9 (2017) 12609–12617.
- [53] X. Song, S. Li, J. Dai, L. Song, G. Huang, R. Lin, J. Li, Gang Liu, H. Yang, Polyphenol-inspired facile construction of smart assemblies for ATP- and pH-responsive tumor MR/Optical imaging and photothermal therapy, *Small* 13 (2017) 1603997.
- [54] X. Li, K. Luo, X. Lin, C. Zhu, Multifunctional ultra-small nanocomplexes capping mesoporous silica nanoparticles for multimodal imaging and chemo-photothermal therapy, *ChemNanoMat* 5 (2019) 1115–1122.
- [55] R.K. Feller, A.K. Cheetham,  $\text{Fe(III)}$ ,  $\text{Mn(II)}$ ,  $\text{Co(II)}$ , and  $\text{Ni(II)}$  3,4,5-trihydroxybenzoate (gallate) dihydrates; a new family of hybrid framework materials, *Solid State Sci.* 8 (9) (2006) 1121–1125.
- [56] P.K. Jain, K.S. Lee, I.H. El-Sayed, M.A. El-Sayed, Calculated absorption and scattering properties of gold nanoparticles of different size, shape, and composition: applications in biological imaging and biomedicine, *J. Phys. Chem. B* 110 (2006) 7238–7248.
- [57] C. Bohren, D. Huffman, Absorption and scattering by a sphere. In absorption and scattering of light by small particles, Wiley-VCH Verlag GmbH: Weinheim (1983) 82–129.
- [58] K. Jiang, D.A. Smith, A. Pinchuk, Size-dependent photothermal conversion efficiencies of plasmonically heated gold nanoparticles, *J. Phys. Chem. C* 117 (51) (2013) 27073–27080.
- [59] J. Bai, X. Jia, W. Zhen, W. Cheng, X. Jiang, A facile Ion-doping strategy to regulate tumor microenvironments for enhanced multimodal tumor theranostics, *J. Am. Chem. Soc.* 140 (2018) 106–109.
- [60] C. Xu, Y. Wang, H. Yu, H. Tian, X. Chen, Multifunctional theranostic nanoparticles derived from fruit-extracted anthocyanins with dynamic disassembly and elimination abilities, *ACS Nano* 12 (2018) 8255–8265.
- [61] K. Yang, J. Wan, S. Zhang, Y. Zhang, S.T. Lee, Z. Liu, In vivo pharmacokinetics long-term biodistribution, and toxicology of PEGylated graphene in mice, *ACS Nano* 5 (2011) 516–522.
- [62] J. Han, G. Liang, D. Xing, A pH-sensitive zwitterionic iron complex probe with high biocompatibility for tumour-specific magnetic resonance imaging, *Chem. Eur. J.* 25 (2019) 8353–8362.